Journal of Materials Chemistry C

ROYAL SOCIETY OF CHEMISTRY

PAPER

View Article Online
View Journal | View Issue

Check for updates

Cite this: J. Mater. Chem. C, 2021, 9, 4628

A roadmap for laser optimization of Yb:$Ca_3(NbGa)_5O_{12}$-CNGG-type single crystal garnets†

J. O. Álvarez-Pérez, J. M. Cano-Torres, A. Ruiz,‡ M. D. Serrano, C. Cascales and C. Zaldo *

The continuous wave laser performance of Yb-doped $Ca_3(NbGa)_5O_{12}$-CNGG-type disordered single crystal cubic garnets has been analyzed on the statistical basis of 26 crystals grown by the Czochralski method under different conditions. The low purity of the $CaCO_3$ chemical used for phase synthesis is the major source of colour induced by non-correlated visible and red-near infrared optical absorptions, but the centres responsible for this colouration have a very minor impact on Yb^{3+} laser performance. The use of high purity ($\geq$99.99%) Yb_2O_3 is essential to preserve the radiative properties of the Yb^{3+} laser. The Yb segregation coefficient in CNGG amounts to $S_{Yb} = 1.12 \pm 0.11$. Up to 20% of Ca^{2+} in the dodecahedral garnet site can be substituted by Na^+ and Yb^{3+} with $S_{Na} = 0.39 \pm 0.05$ and $S_{Yb} = 1.34 \pm 0.09$, respectively, *i.e.* Na promotes Yb incorporation. In contrast, tetrahedral Li^+ reduces Yb incorporation to $S_{Yb} = 0.88 \pm 0.07$. The Yb^{3+} peak absorption cross section in CNGG amounts to $\sigma_{ABS}(\lambda = 971.7\text{nm}) = 1.97 \pm 0.32 \times 10^{-20}$ cm^2. σ_{ABS} is sensitive to Na and Li incorporation but no evidence of significant emission or gain cross section changes is found indicating that the majority Yb^{3+} centre is responsible for the observed fluorescence. Correspondingly, laser performance of crystals containing up to 15 at% of Yb shows only a slight improvement in Li-modified Yb:CLNGG crystals, associated with better crystalline quality. In them laser tuning extends in an unprecedented range up to 60 nm, even beyond 1080 nm in Li and Na co-modified crystals. 7–8 at% Yb doping of Li-modified CLNGG crystals with ≈95% pump absorption show large laser slope efficiency along with maximized output power.

Received 5th December 2020,
Accepted 24th February 2021

DOI: 10.1039/d0tc05718e

rsc.li/materials-c

Open Access Article. Published on 22 March 2021. Downloaded on 4/26/2024 4:27:57 AM.
This article is licensed under a Creative Commons Attribution-NonCommercial 3.0 Unported Licence.

1. Introduction

In the past years there has been very intense and prolific research into the development of mode-locked ultrashort (fs) laser pulses both in oscillators and amplifiers.[1–4] Different gain media, including dyes dispersed in liquids, semiconductors, optical fibers and solid state technologies, have been used for this purpose. Even nowadays, the latter is the only option for high peak/average (>1 MW/>100 GW) laser powers.[5] In turn, high power solid state lasers comprise glass, single crystal and ceramics optical gain media. In chronological order, single crystals replaced glass due to the low thermal conductivity of the latter, and ceramics are gaining use due to their better mechanical properties and superior processing versatility than single crystals.

Although the technology of Ti-sapphire (Ti-sa) laser systems is very well established and presently it is the single crystal of reference for production of fs laser pulses, more recently Yb^{3+} lasers have attracted a lot of attention because they are in-band pumped with InGaAs diode lasers (DL), the quantum defect of Yb^{3+} is very small alleviating the thermal problems generally encountered in most solid state lasers, and Yb^{3+} has no excited state optical absorption losses. These are large advantages for the power scalability of the laser systems.

Ultrashort laser pulses require optical gain media with a large fluorescence bandwidth. Most trivalent lanthanides (Ln^{3+}) do not fulfil this requirement due to the inner character of the $4f^n$ orbital, but the situation is more favourable for Tm^{3+} ($4f^{12}$) and Yb^{3+} ($4f^{13}$). The near to full filling of the 4f orbitals for these latter ions favours electron interactions with lattice vibrations and their f–f spectroscopic bands are much broader than those observed for the rest of the Ln^{3+}. In spite of this fact conventional

Instituto de Ciencia de Materiales de Madrid, Consejo Superior de Investigaciones Científicas, c/Sor Juana Inés de la Cruz 3, 28049 Madrid, Spain.
E-mail: cezaldo@icmm.csic.es

† Electronic supplementary information (ESI) available: (i) Laser setup. (ii) Summary of previous laser achievements. (iii) Crystal growth, analysis of phases present in solid state synthesized precursors and crystal melting. (iv) Inventory of crystals. (v) Crystallographic data. (vi) WDXRF of Na. (vii) Effect of thermal annealing on OA. (viii) σ_{ABS} of CNNGG. (ix) Low temperature Yb^{3+} spectroscopy. (x) Yb^{3+} lifetime measurements. (xi) Role of Yb_2O_3 purity on laser performance. (xii) Effect of air annealing on Yb^{3+} lifetime. See DOI: 10.1039/d0tc05718e

‡ In memoriam of Ana Ruiz y Ruiz de Gopegui (Avilés, July 31st 1960 – Madrid, February 14th 2021).

This journal is © The Royal Society of Chemistry 2021

Open Access Article. Published on 22 March 2021. Downloaded on 4/26/2024 4:27:57 AM.
This article is licensed under a Creative Commons Attribution-NonCommercial 3.0 Unported Licence.

Yb-doped single crystals and ceramics, such as Yb:YAG in which Yb (and other Ln^{3+}) has a unique crystallographic position and environment, show time-bandwidth limited laser pulses with a duration longer than 100 fs.[6] Only when the spontaneous wavelength emission was hindered could Yb:YAG break down the 100 fs barrier,[7] but at the cost of reduced efficiency.

Solid state lasers have been demonstrated for years using either glass or single crystal doped hosts. Although the newer transparent ceramics technology[8–10] is gradually replacing the above hosts, there are still many applications which benefit from the use of single crystals, for instance in TW–PW short pulsed lasers the depolarization losses are minimized by crystal orientation[11,12] which cannot be achieved in ceramics, when UV Xe lamp pumping is required permanent solarisation of the presently developed YAG ceramics may appear,[13] or the larger Rayleigh light scattering of ceramics in the visible region may limit laser implementation in this spectral range. Furthermore, despite grain-oriented anisotropic fluorapatite ceramics being produced with limited optical transmittance for laser applications,[14,15] large cross section laser ceramics are basically restricted to optically isotropic media, *i.e.* cubic materials, which limits host options for optical bandwidth engineering.

The so called "*disordered*" crystals are presently being actively investigated as an alternative to enlarge the fluorescence bandwidth of Yb^{3+} and other Ln^{3+}, with the aim of achieving shorter laser pulses. In disordered crystals a variety of crystalline environments around the Ln^{3+} induces further inhomogeneous broadening with regard to conventional ordered crystals. In fact, this goal has been pursued first in single crystal and later in ceramic garnet hosts by isovalent substitutions, for instance in Yb:$(YGd_2)Sc_2(GaAl_2)O_{12}$ media reaching 112 fs pulses.[16]

The $\{Ca\Diamond\}_3[NbGa\square]_2(GaNb¤)_3O_{12}$ cubic garnet (hereafter shortened as CNGG. $\Diamond$, $\square$, and ¤ are cationic vacancies at the corresponding sites) is an outstanding disordered crystal since laser pulses as short as 45 fs have been demonstrated in a 10 at% Yb-doped crystal of this class,[17] and it has the potential to be developed as transparent ceramics, although the attempt so far reported was not successful.[18] Room temperature thermal conductivity of CNGG is intermediate, reaching 4.4 W m^{-1} K^{-1} in undoped CNGG and 3.63 W m^{-1} K^{-1} for Li-modified 7.57 at% Yb:CLNGG.[19] Although a minor ($<5 \times 10^{18}$ cm^{-3}) amount of Yb^{3+} can be found in the octahedral [16*a*] site of this garnet[20] the majority of Yb sits at the dodecahedral {24*c*} site, which is also occupied by Ca^{2+} and eventually with a small amount (1.5%) of {$\Diamond$} vacancies, being surrounded by several oxygen polyhedra: four other nearest dodecahedra {24*c*}, four corner-sharing octahedra [16*a*] and six tetrahedra (24*d*), four of the latter sharing corners and the two others, at the shortest distance, sharing edges. In undoped CNGG the octahedral site is mostly filled by Nb^{5+} ($\approx$62%) with a minor amount of Ga^{3+} ($\approx$37%) and [$\square$] vacancies ($\approx$0.3%), while the tetrahedral site is mostly filled by Ga^{3+} ($\approx$82%) with minor occupancy of Nb^{5+} ($\approx$10%) and (¤) vacancies ($\approx$8%). These occupancies are further sensitive to the Yb doping and to the incorporation of crystal modifiers (non-optically active dopants, such as Na^+ or Li^+). The crystalline complexity provides a large number of oxygen and cationic environments around Yb^{3+} with a large impact on its optical band broadening. Furthermore, Na[21] and Li[22,23] CNGG modifications (hereafter CNNGG and CLNGG crystals, respectively) have been also developed. Na^+ enters in the dodecahedral site, potentially helping in the charge compensation of Ca^{2+} substitution by Yb^{3+},[21] while Li^+ exclusively sits at the tetrahedral sites, removing tetrahedral cationic vacancies.[19]

Laser characterization of Yb:CNGG-type crystals has been demonstrated in continuous wave (cw), Q-switched and mode-locked operation regimes. For a comprehensive description of the work so far reported see the ESI,† Table S1. In particular, rather high laser output powers, 5–10 W, have been obtained in cw operation, as well as short (45 fs) laser pulses in mode-locked operation under DL pumping. However, the activity and conclusions are limited by the scarce variety of available crystals, most often limited to only 5 at% Yb nominal doping. On the other hand, the spectroscopic results so far reported are to some extent contradictory, for instance the Yb^{3+} $0 \rightarrow 0'$ maximum absorption cross section (at $\lambda \approx 972$ nm) varies in the σ_{ABS} = 1.4–3.8 $\times$ 10^{-20} cm^2 range while its full width at half maximum (FWHM) has been reported in the 2.6–15 nm range and the reported ratio between absorption cross sections at λ = 972 and λ = 933 nm varies in the 1–2.8 range. Furthermore, the average output power achieved for the shortest pulses is modest, $\approx$30 mW. In some cases improvements in the laser performance associated with Li or Na modifications have been claimed,[17,24] but some of these conclusions are doubtful since we shall show that the actual crystal concentration of Na is much lower than previously assumed. Other aspects, such as the influence of crystal colouration, purity of chemical reagents, or the Yb concentration and associated pump absorption on laser performance, have been mostly ignored.

In the present work by using 26 crystals (24 of them doped with Yb) with different compositions and growth procedures we extend the knowledge about optimal material and experimental conditions for cw Yb^{3+} laser operation, which is a required first step for scaling power in mode-locked laser operation. Also, the improvement of the knowledge of the physicochemical properties of the material may help in successful ceramics development in the future. We carefully monitor Na incorporation into Yb:CNNGG crystals and the Yb concentration for unmodified and Li- or Na-modified crystals. We probe that laser operation occurs up to $\approx$15 at% of Yb doping of the dodecahedral {24*c*} site, opening the possibility of thin-disk laser designs.[25,26] Among the different material and growth variables considered, the most relevant ones are the $CaCO_3$ reagent purity which determines crystal colouration, the Yb concentration and Yb_2O_3 reagent purity which determines pump absorption and Yb^{3+} fluorescence quantum yield, the crystal mosaicity which is found to be similar to that of the commercial Yb:YAG crystal, as well as the presence of crystal modifiers. The impact of these variables on the Yb^{3+} laser performance is analysed in detail. Finally, we show that the oxygen content in the CNGG-type Czochralski grown crystals is virtually the same as that of the stoichiometric formula and apparently it cannot be modified by after growth oxidation annealing near the melting point, but vacuum thermal annealing even at moderate temperature

Open Access Article. Published on 22 March 2021. Downloaded on 4/26/2024 4:27:57 AM.
This article is licensed under a Creative Commons Attribution-NonCommercial 3.0 Unported Licence.

(≈800 °C) leads to generalized Ga loss which could be the origin of the failure in previous ceramic processing.

2. Experimental techniques

CNGG-type single crystals were grown from melts of precursor ceramic powders synthesized by solid state reaction. Differential scanning calorimetry (DSC) measurements of these precursor powders and grown crystals were made with Setaram equipment, model SETSYS Evolution. Two consecutive 10 °C × min^{-1} heating/cooling cycles in air were carried out in all cases. These precursor powders were further characterized by powder X-ray diffraction (XRD) θ–2θ scans using a Bruker D8 Advance diffractometer operated with a Cu Kα source and a Lynxeye position sensitive detector.

An oxidative atmosphere, either air or O_2, and Pt crucibles were used for the Czochralski growth. Crystal growth details can be found in our previous works.[19,21] Rocking curves of the 100 XRD of CNGG-type crystals were recorded at room temperature in a Texture Analysis Diffractometer Bruker D8 Advance with Cu Kα radiation.

The incorporation of Yb and Na into the crystal was determined by X-ray fluorescence analyses in a JEOL Superprobe JXA-8900 Electron Probe Micro Analyzer (EPMA). The ZAF method[27] and CaO, Nb_2O_5, Ga_2O_3, Yb_2O_3 and Na_2O standards were used. Na concentration was also evaluated by Wavelength Dispersive X-Ray Fluorescence (WDXRF) using a MagiX sequential spectrometer and methods described in a previous work.[28] For the latter purpose specific Na standards were developed for calibration as explained in the ESI,† see Fig. S5, and the interference between Ga and Na X-ray emissions was explicitly considered, see Fig. S6 (ESI†). Furthermore, single crystal X-ray diffraction (scXRD) refinements of the crystallographic structure, at least in crystals having the largest Yb concentration for each CNGG, CNNGG and CLNGG crystal series, were performed. Details of the scXRD equipment and procedures used can be found in the ESI† and in our previous works.[19,21] When required, Yb concentrations were also calculated from the integrated optical absorption of Yb^{3+} taken as reference EPMA measurements. Table S3 (ESI†) summarizes the growth conditions, composition and other physical properties of the 26 used crystals.

Optical absorption (OA) was recorded in a Varian 5E spectrophotometer with a spectral resolution of 0.15 nm for $\lambda \approx$ 900–1150 nm and 0.2 nm for $\lambda \approx$ 300–850 nm. The spectra were acquired with a wavelength scanning step of 0.05–0.1 nm and 1–5 s of integration time. To decrease acquisition noise, each near infrared (NIR) spectrum was the average of ten acquisitions. Furthermore, for each crystal composition several sample thicknesses were compared to assure the linear response of the equipment, and thick samples (>10 mm) were used to record the weak Yb^{3+} OA in the λ = 980–1150 nm spectral region. Photoluminescence (PL) was excited with a Ti-sa laser, dispersed using a Czerny–Turner SPEX monochromator (f = 34 cm) and detected with a 77 K cooled Ge photodiode. All NIR PL measurements were corrected by the spectral response of the equipment. The Yb lifetime was determined from the intensity decay of the λ = 1021 or 1035 nm PL excited with a MOPO laser system tuned at λ = 971 or 972 nm, this PL was dispersed using the above-described monochromator, detected with a Peltier-cooled Hamamatsu photomultiplier model H10330A-75, and recorded with Lecroy 200 MHz or Tektronix 500 MHz oscilloscopes. For all these spectroscopic measurements the sample temperature was set in the 6–300 K range by using a closed-cycle He cryostat equipped with a Lake Shore temperature controller.

Laser properties of the crystals were assessed in a z-shaped optical resonator sketched in the ESI,† Fig. S1. A lens (f = 80 mm) focuses onto the sample the TEM00 mode of a cw Ti-sa laser. It generates a focus with a diameter of 62 μm and a depth of focus $2z_0 \approx$ 4 mm. T_{OC} = 1, 2.5, 5 and 10% output coupler transmissions were used. Laser spectral distribution was assessed with an APE laser spectrometer, model WaveScan. Uncoated samples were glued with silver paste to a water-cooled (16 °C) copper holder. Samples were set perpendicularly to the pumping beam and the sample Fresnel reflection was evaluated from the refractive index of the crystal.[19] Laser tuning was obtained by inserting a SF10 prism in the cavity.

3. Results

3a. Crystal growth, composition and crystallography

As a preliminary step for crystal growth, the melting nature of $(Ca_{1-2x}Yb_xNa_x)_3(Nb_{0.3375}Ga_{0.6375})_5O_{12}$ precursor powders synthesized by solid state reaction (two steps of heating to 1330 °C for 6 h with intermediate grinding) was studied by DSC. Results are shown and discussed in detail in the ESI.† For undoped CNGG only a single endo/exothermic peak was observed upon two consecutive heating/cooling cycles, see Fig S2a (ESI†). This situation is maintained up to <20 at% of total Yb + Na cooperative substitution in the garnet formula. For ≥20 at% of Ca substitution new peaks at a temperature lower than that corresponding to the garnet melting are observed in the first and second DSC cycles, see Fig. S2b (ESI†). Thus, it can be anticipated that the total Na + Yb limit for melt stability occurs for Ca substitution in the garnet dodecahedral position of ≈20 at%, even lower for non-modified Yb:CNGG precursor powders.

Correspondingly, Yb:CNGG crystals were obtained with good optical quality up to 15 at% of Yb concentration in the melt. Likewise, up to 30 at% of Na in the melt (8.78 at% of Na in the crystal) could be used to grow Na-modified ≈9.4 at% Yb:CNNGG crystals. Furthermore, Li - and Li + Na-modified 8 at% (in the melt) Yb:CLNGG and Yb:CLNNGG crystals were also grown. These crystals have been grown using Yb_2O_3 of 99.9%, 99.99% or ≥99.998% purity. $CaCO_3$ with 99.5% or 99.99% of purity was used. Other used reagent purities were 99.5% and 99.997% for Na_2CO_3, 99% and 99.997% for Li_2CO_3, 99.9% or 99.99% for Nb_2O_5 and 99.99% for Ga_2O_3. Some crystals were grown in a pure oxygen (O_2) atmosphere and others in air. Further DSC analyses of the grown single crystals show that Yb and Li incorporations increase the melting temperature while Na modification significantly decreases it, see the ESI† Table S2.

 This journal is © The Royal Society of Chemistry 2021

Open Access Article. Published on 22 March 2021. Downloaded on 4/26/2024 4:27:57 AM.
This article is licensed under a Creative Commons Attribution-NonCommercial 3.0 Unported Licence.

In our previous scXRD analyses[21] of CNGG-type crystals, combined with high resolution powder neutron diffraction data for Li-modified CLNGG crystals,[19] an oxygen stoichiometric composition was assumed for the analysis. Taking into account that some oxide single crystals may be oxygen deficient, as established by careful scXRD refinements in alternative materials,[29,30,31] the oxygen occupancy factor (OF) is now refined for undoped CNGG and selected Yb:CNGG-type (either non-modified or modified with Na) crystals to assess its influence on crystal stoichiometry. Structure refinements have been performed in the cubic space group $Ia\bar{3}d$ (No. 230), and they include atomic coordinates, the evaluation of cationic and vacancy distributions over dodecahedral {24*c*}, octahedral [16*a*], and tetrahedral (24*d*) garnet crystal sites, and anisotropic thermal displacements. These analyses provide an alternative estimation of crystal compositions, as well as unit cell parameter and interionic distances. A selection of the obtained results is included in Table 1. These results indicate that the studied CNGG-type crystals do not present oxygen deficiency, moreover their comparison with previous data from structure analyses that did not include oxygen OF refinements reveals differences only within the estimated precision in cationic and vacancy distributions. Further details of scXRD refinements as well as crystal data are included in the ESI,† Tables S4–S7.

With reference to undoped CNGG crystal the substitution of Ca^{2+} by Yb^{3+} induces a reduction of the cell volume. This is compensated when Na^{+} is simultaneously incorporated in the dodecahedral site. Cationic vacancies over the dodecahedral and octahedral sites are virtually eliminated by the Yb and Na incorporation, but vacancies on the tetrahedral site are reduced to a lesser extent. These are only largely eliminated by Li modification.

Fig. 1a and b show the relationship between in-the-melt and in-the-crystal Yb and Na concentrations, respectively. Considering all techniques used, the Yb segregation coefficient in CNGG is $S_{Yb} = 1.12 \pm 0.11$. When Na is added to the melt in the same amount as Yb, the segregation coefficient of the latter increases slightly up to $S_{Yb} = 1.34 \pm 0.09$, while it reduces to $S_{Yb} = 0.88 \pm 0.07$ for Yb:CLNGG crystals, which shows the benefit of Na co-doping for Yb incorporation. These results agree qualitatively with those obtained in ref. 32, $S_{Yb} = 1.19$ for 10 at% Na: 10 at% Yb:CNNGG and $S_{Yb} = 1.07$ for 10 at% Na: 10 at% Yb:CLNNGG, which confirms that Li modification reduces Yb incorporation. On the other hand, the segregation coefficient for Na is $S_{Na} = 0.39 \pm 0.05$. The difficult incorporation of Na is the likely reason for there only being a small difference between S_{Yb} of Yb:CNGG and Yb:CNNGG crystals and it induces a Na-rich melt as the crystal growth proceeds, which at some point degrades the melt composition and produces growth instabilities.

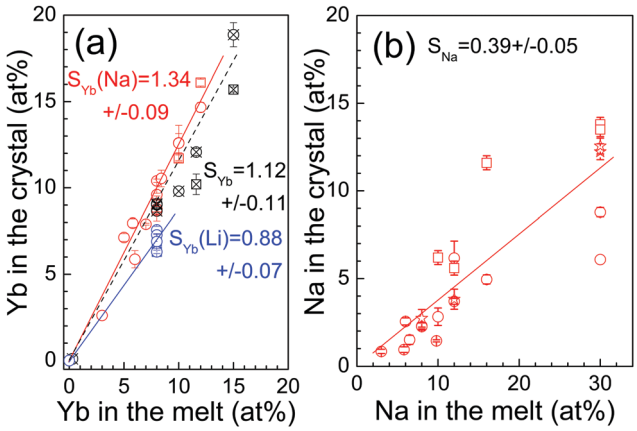

Fig. 1 (a) Yb and (b) Na segregation coefficients (*S*) in CNGG-type single crystals. Circles are EPMA results, stars WDXRF results and squares those of scXRD refinements. Crossed black symbols are for Yb:CNGG, red symbols are for Yb:CNNGG and blue symbols are for Yb:CLNGG crystals. Lines are best fits of the experimental results.

Although single crystals appear macroscopically free of defects, at the microscopic scale they have a mosaicity characterized by the angular width of a selected X-ray reflection in rocking curve experiments. We first analysed the 100 reflection of a 10 at% Yb:YAG acquired from a commercial laser crystal manufacturer. The full width at half maximum (FWHM) of the reflection was $\Delta\theta = 0.0153$ deg. This was clearly larger than the instrumental resolution that was determined with a 111 Si standard as 0.0071 deg. Fig. 2 shows selected 100 rocking curves obtained for analyzed CNGG-type crystals, including Nd, Er and Yb dopants as well as Li and Na modifiers. The width of the X-ray reflection falls within the

Table 1 Summary of crystallographic results from scXRD refinements of CNGG-type cubic ($Ia\bar{3}d$, $Z = 8$) garnets. *a* = lattice parameter. OF = occupancy factors. Na/Yb and Li atomic melt compositions (at%) are referenced to the octahedral and tetrahedral sites, respectively. *Previously available data without oxygen OF refinement

		OF											
		{24*c* dodecahedral site}				[16*a* octahedral site]			(24*d* tetrahedral site)				96h
Melt composition (at%)	*a* (Å)	Ca^{2+}	Yb^{3+}	Na^{+}	◊	Nb^{5+}	Ga^{3+}	□	Ga^{3+}	Nb^{5+}	Li^{+}	¤	O^{2-}
CNGG	12.4969(1)	0.987(6)	—	—	0.013	0.623(4)	0.374(4)	0.003	0.82(4)	0.10(4)	—	0.08	0.994(8)
11.6Yb: CNGG	12.4548(3)	0.868(2)	0.102(2)	—	0.03	0.63(2)	0.34(2)	0.03	0.922(4)	0.003(4)	—	0.075	0.999(6)
Li-Modified													
CLNGG*	12.50657(2)	0.998(5)	—	—	0.002	0.66(3)	0.34(3)	0	0.842(4)	0.052(4)	0.079(14)	0.027	1
9.2Li:8Yb:CLNGG*	12.48228(2)	0.931(4)	0.069(4)	—	0	0.67(3)	0.33(3)	0	0.810(3)	0.069(3)	0.111(15)	0.01	1
Na-Modified													
30Na:8Yb: CNNGG	12.4883(1)	0.814(4)	0.051(1)	0.135(4)	0	0.550(4)	0.450(4)	0	0.825(4)	0.085(4)	—	0.090	0.999(6)
16Na:8Yb:CNNGG	12.4842(1)	0.791(4)	0.093(1)	0.116(4)	0	0.661(4)	0.339(4)	0	0.93(4)	0.01(3)	—	0.06	0.997(7)
12Na:12Yb:CNNGG	12.4611(1)	0.783(4)	0.161(2)	0.056(4)	0	0.773(4)	0.227(4)	0	0.94(4)	0.02(4)	—	0.04	0.993(8)
10Na:10Yb:CNNGG	12.4618(1)	0.783(4)	0.117(2)	0.059(4)	0.041	0.659(4)	0.341(4)	0	0.918(4)	0.022(4)	—	0.060	1.01(1)

Open Access Article. Published on 22 March 2021. Downloaded on 4/26/2024 4:27:57 AM.
This article is licensed under a Creative Commons Attribution-NonCommercial 3.0 Unported Licence.

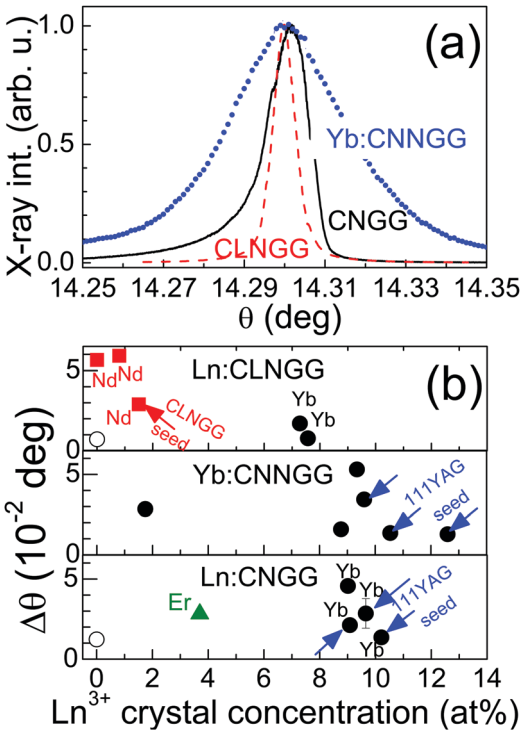

Fig. 2 (a) 100 rocking curves of undoped CNGG (black solid line), Li-modified CLNGG (dashed red line) and 2.3 at% Na: 9.6 at% Yb:CNNGG (dotted blue line) crystals. (b) Summary of mosaicity ($\Delta\theta$ is the FWHM of the rocking curve) degree of CNGG-type crystals for different lanthanide concentrations. Undoped crystals, empty symbols; Nd-doped crystals, full red squares; Er-doped crystals, full green triangles; and Yb-doped crystals, full black circles. The crystals were either spontaneously nucleated on a platinum wire (no arrow label), nucleated on 111 YAG crystalline seeds (blue arrow labels) or on undoped 111 CLNGG crystal (red arrow label).

$\Delta\theta$ = 0.0065–0.06 deg range depending on the incorporated cations and growth conditions. Undoped CNGG has $\Delta\theta$ = 0.0123 deg. The smallest mosaicity was found for undoped Li-modified CLNGG, $\Delta\theta$ = 0.0065 deg, *i.e.* in the limit of our instrumental resolution. The incorporation of Yb supposes in all cases a moderate increase of the crystal mosaicity with regards to the corresponding undoped host, which was most evident in Na-modified Yb:CNNGG crystals, see Fig. 2a. However, significant differences are found if the seed used for growth is taken in consideration. Crystals grown using 111 YAG seeds generally have smaller $\Delta\theta$ mosaicity values than those spontaneously nucleated on platinum wires.

Li-modified Yb:CLNGG crystals exhibit a mosaicity similar to that of commercial Yb:YAG with similar Yb content, even when these crystals were spontaneously nucleated on Pt wire. The incorporation of Nd^{3+} (larger ionic radii than Yb^{3+}) in CLNGG leads to a rapid increase of the mosaicity even for low Nd concentrations, <1.5 at% in the melt, but also in this case the use of a CLNGG crystalline seed reduced significantly the mosaicity, see Fig. 2b.

3b. Crystal colouration

Grown CNGG-type crystals show different colours from intense green to pale yellow, and exceptionally they appear colourless, see Fig. 3a insets for two extreme examples of the crystal colouration obtained. This colouration is commonly reported in the literature for CNGG-type crystals grown by the Czochralski method.[21,33–35] Two different OA features determine the observed crystal colour, see Fig. 3a. On one hand a complex but relatively weak OA is present in the λ = 580–800 nm Red-NIR region and on the other hand a pre-edge visible (VIS) OA overlapping the band gap optical transition is observed for λ < 500 nm. The difference between the VIS OA observed in highly and lowly coloured crystals is a band with maximum at λ = 350 nm, see dashed line in Fig. 3a.

Fig. 3b shows a plot of the OA in the VIS *versus* that in the Red-NIR region for the different CNGG-type grown crystals. It is obvious that VIS and Red-NIR OA are not correlated, *i.e.* they correspond to different optical centres. Crystals grown in a pure oxygen atmosphere, labelled as O_2 in Fig. 3b, do not show lesser colouration than those grown in air, which in accord with the above presented crystallographic study (oxygen OF ≈ 1) suggests that oxygen deficiency is not the origin of the observed colouration. A similar conclusion is reached from thermal annealing in air or in vacuum of CNGG-type crystals, see the ESI,† Fig. S7 and S8. Crystals annealed to 1340 °C (*i.e.* only

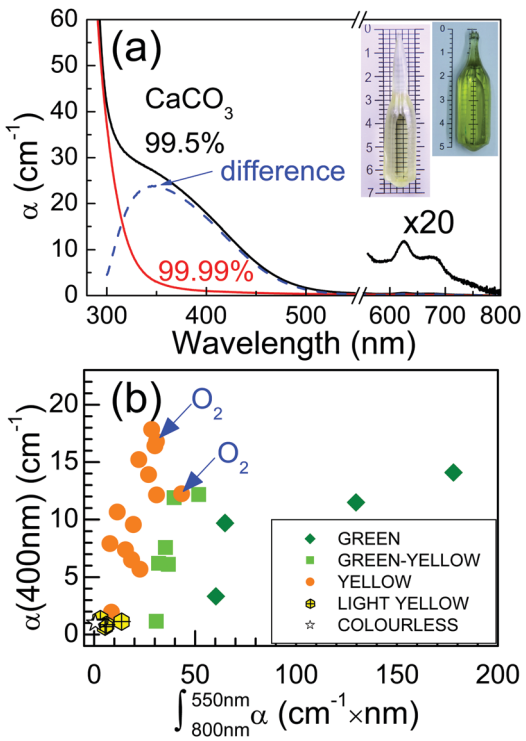

Fig. 3 (a) Comparison of the room temperature optical absorption of undoped CNGG (continuous black line, scaled by ×20 in the Red-NIR region) and 0.08 at% Yb:CNGG (continuous red line) single crystals grown using 99.5% (green crystal in the right inset) and 99.99% (pale yellow crystal in the left inset) $CaCO_3$, respectively. The dashed line shows the difference in VIS OA between both crystals. (b) Plot of the OA coefficient, α, at λ = 400 nm *versus* the Red-NIR integrated (from λ = 550 to 800 nm) OA coefficient for the different CNGG-type crystals studied. The symbol colour mimics the crystal colour. Crystals were grown in an air atmosphere (not labelled) or in flowing pure oxygen (blue arrows and O_2 labels).

This journal is © The Royal Society of Chemistry 2021

Open Access Article. Published on 22 March 2021. Downloaded on 4/26/2024 4:27:57 AM.
This article is licensed under a Creative Commons Attribution-NonCommercial 3.0 Unported Licence.

≈100 °C below the melting temperature) for 48 h do not show any significant modification of the OA associated to the colouration, and crystals reduced for 50 h in vacuum (2.5×10^{-2} mbar) up to 900 °C don't show significant changes of the bulk colour, although in this case the crystal surface degrades with evident Ga loss, see Fig. S9 (ESI†).

Furthermore, crystal colouration is not exclusive to Yb-doped crystals, it also appears in undoped/unmodified CNGG crystals, so it is not directly related to the purity of used Yb_2O_3. Although low purity reagents (99.5% Na_2CO_3 and 99% Li_2CO_3) were used to grow some crystals, see Table S3,† their small required amount makes it unlikely that they were the main source of colouration. The use of low purity 99.5% $CaCO_3$ precursor is the main cause of the observed crystal colouration. According to the Analysis Certificate of the 99.5% $CaCO_3$ Alfa Aesar supplier, traces of transition metals are present: Fe, 0.0003%; Ba, 0.0008%; Sr, 0.003%; and Mg, 0.0012%. The presence of these contaminants in our crystal was tested by EPMA but, if present, their concentration is below the detection limit of the technique. Nevertheless, Fe garnets have intense OA bands in the VIS region,[36] thus it seems to us likely that the VIS pre-edge absorption could be related to residual Fe impurities, as also suggested for YAG.[37] The Red-NIR bands are maybe ascribed to localized electric charge trapped near cationic vacancies present in the structure,[38] thus they decrease as vacancies are removed, for instance by doping with Li.

3c. Yb^{3+} optical cross sections

The Yb^{3+} absorption cross section, defined as $\sigma_{ABS} = \alpha/[Yb]$ (where α is the Yb^{3+} absorption coefficient and [Yb] is the Yb^{3+} density in the crystal) describes the crystal efficiency for absorption of the optical pumping. In the case of cubic garnet crystals the OA is isotropic. A correct evaluation of σ_{ABS} is essential in the assessment of laser performance since the emission and gain cross sections (the latter characterizing the efficiency of three level lasers) are obtained from it. For Yb:CNGG we have used seven crystals with different Yb concentrations to average the results, while for Na-modified Yb:CNNGG only the crystal with maximum Na concentration (12.23 at% Na and 7.13 at% Yb in the crystal) is used, and two different crystals with 7.57 and 7.28 at% Yb in the crystal were averaged for the Li-modified Yb:CLNGG case. The Yb incorporation to the CNGG lattice shrinks the garnet cell volume (see Table 1) increasing the Yb density. This effect has been taken into account explicitly in our σ_{ABS} calculations by using actual cell volumes obtained by XRD analyses for each used crystal. The same procedure has been also used for Yb:CLNGG crystals, however for the Na-modified Yb:CNNGG the cell size reduction induced by Yb^{3+} is largely compensated by the increase induced by the bigger ionic size of Na^+, thus the volume cell of CNGG was used. Fig. 4 shows the σ_{ABS} results obtained at room temperature.

The Yb^{3+} electronic configuration consists only of the ground $^2F_{7/2}$ and one excited $^2F_{5/2}$ multiplets whose degeneracy is lifted by the lattice crystal field into four (m_J = 0, 1, 2, 3) and three (m_J = 0′, 1′, 2′) Stark levels, respectively. Consequently, its OA spectrum is composed of a prominent Yb^{3+} 0 → 0′ band

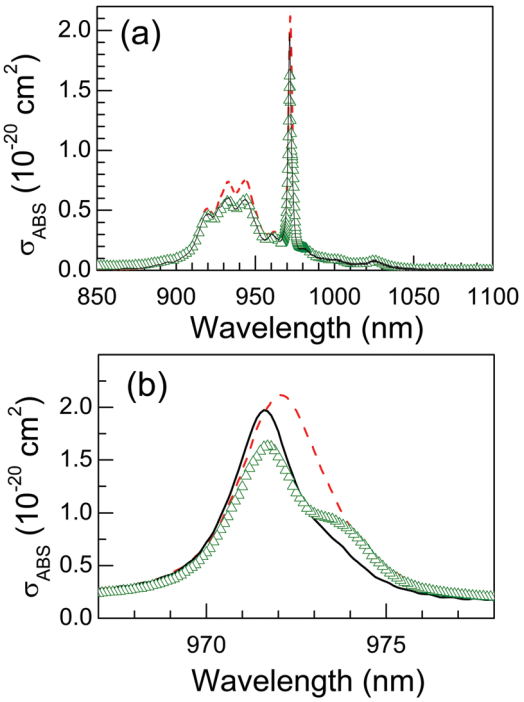

Fig. 4 Room temperature Yb^{3+} absorption cross sections, σ_{ABS}, of CNGG-type garnet crystals. Average of seven Yb:CNGG crystals, solid black line. 12.23 at% Na-modified 7.13 at% Yb:CNNGG, green triangles. Average of two Li-modified Yb:CLNGG crystals, dashed red line. (a) Long spectral range. (b) Detail of the Yb^{3+} σ_{ABS} corresponding to the 0 → 0′ transition.

near to λ = 971.7 nm and of Yb^{3+} 0 → 1′,2′ related bands at λ = 944.2, 933 and 922 nm. The observation of more bands than expected should be related to the coexistence of several different crystalline environments around Yb and/or phonon coupling effects. Furthermore, at 300 K other replica bands with minor intensity are observed at the low energy side of these and ascribed to thermally assisted Yb^{3+} 1,2,3 → 0′,1′,2′ transitions. The most significant differences between Yb:CNGG and Na- or Li-modified crystals are: (a) The σ_{ABS} ratio between λ = 971.7 nm and λ = 933 nm evolves from Yb:CNGG, σ_{ABS}(971.7 nm)/σ_{ABS}(932.7 nm) = 3.19, to σ_{ABS}(971.8 nm)/σ_{ABS}(933 nm) = 2.85 in Yb:CNNGG, and to σ_{ABS}(972.1 nm)/σ_{ABS}(933 nm) = 2.86 for Yb:CLNGG. In the case of Na-modified Yb:CNNGG crystals the decrease is due to the appearance of a new Yb^{3+} 0 → 0′ absorbance at λ = 973.5 nm, see Fig. 4b and Fig. S10.† In contrast, the decrease observed for the Yb:CLNGG crystal is mainly due to an enhancement of the Yb^{3+} 0 → 1′,2′ bands at λ = 944 and 933 nm. (b) The shape of the Yb^{3+} 0 → 0′ band in CNGG crystals at room temperature is observed to be rather symmetric with a FWHM = 2.23 nm, but this changes with crystal modifications. For Na modification the aforementioned band at λ = 973.5 nm appears, and the FWHM of the overlapped bands increases to 3.65 nm, while for Li modification the maximum of the Yb^{3+} 0 → 0′ band in CLNGG shifts to longer wavelengths, λ = 972.1 nm, and its FWHM increases (with regard to Yb:CNGG) to 3.1 nm. This peak shift is confirmed

Open Access Article. Published on 22 March 2021. Downloaded on 4/26/2024 4:27:57 AM.
This article is licensed under a Creative Commons Attribution-NonCommercial 3.0 Unported Licence.

by the excitation of laser experiments described in later laser results section. (c) The maximum Yb^{3+} σ_{ABS} of Yb:CNGG amounts to 1.97 ± 0.32 × 10^{-20} cm^2. In the 12.23 at% Na-modified Yb:CNNGG peak σ_{ABS} decreases to 1.65 × 10^{-20} cm^2, while in Li-modified CLNGG it increases to σ_{ABS} = 2.12 ± 0.34 × 10^{-20} cm^2. The measured σ_{ABS} peak value of the narrow band at $\lambda \approx 972$ nm greatly depends on the spectral resolution of the measurements. A large interval of values has been reported in the literature, thus the comparison with previous results based on σ_{ABS} value at 933 nm is more reliable. On this basis, our results agree (within 50% of deviation) with the conclusions of ref. 21, 32, 39 and 40 and refute those of ref. 24, 41 and 42. It is also worth noting that despite the disordered nature of CNGG single crystals, the Yb^{3+} peak σ_{ABS} in it is at least twice larger than that found in Yb:YAG, σ_{ABS}(300 K) = 0.8 × 10^{-20} cm^2.[43]

The emission cross section, σ_{EMI}, describes the fluorescence efficiency of the Yb^{3+} ion. Here, we have used the reciprocity method[44] for its calculation as $\sigma_{EMI} = \sigma_{ABS}(Z_l/Z_u)\exp[(E_{zl}-h\nu)/k_BT]$. The partition functions Z_l and Z_u, $Z = \Sigma_k \exp(-E_k/k_BT)$, for the ground ($^2F_{7/2}$) and excited ($^2F_{5/2}$) Yb^{3+} multiplets, respectively, have been calculated from the Stark level (E_k) energies obtained from 6 K OA and PL spectroscopies, see the ESI,† Fig. S11 and S12. Due to the uncertainties for the band to Yb energy level assignment, associated with the multisite character of these crystals, a unique Z_l/Z_u = 1.45 value was used in all cases. E_{zl} is the energy of the Yb^{3+} 0 → 0′ transition, $h\nu$ is the photon energy and k_B is the Boltzmann constant. Even though thick (>1 cm) samples were used to reduce OA measurement uncertainty for λ > 1040 nm, measurements beyond λ > 1060 nm were not reliable. Therefore, the 300 K Yb^{3+} fluorescence normalized at λ = 1027.6 nm was used for the alternative quantification of σ_{EMI} at these long wavelengths. Fig. 5a shows the $\sigma_{EMI}(\lambda)$ distribution obtained for Yb:CNGG and its change in Na- or Li-modified crystals. In all cases σ_{EMI} peaks at λ = 1027.6 nm. Although Yb:CLNGG has a slightly larger peak σ_{EMI} = 1.87 × 10^{20} cm^2 than Yb:CNGG, σ_{EMI} = 1.56 × 10^{20} cm^2, or Yb:CNNGG, σ_{EMI} = 1.62 × 10^{20} cm^2, for λ > 1045 nm all three curves collapse into a single one. Taking into account that spontaneous cw laser operation takes place at λ = 1030–1060 nm, see later sections, Yb:CLNGG may have slightly better cw laser efficiency, but for mode-locked laser operation, typically operated with low transmission output couplers ($T_{OC} \leq 1\%$), the laser emission shifts to larger wavelength values (λ = 1047–1061 nm) and laser performance differences for the three Yb:CNGG crystal types here considered are not anticipated.

An independent assessment of the certainty of the calculated σ_{EMI} can be inferred from the comparison of the experimental and calculated Yb^{3+} radiative lifetime, τ_{RAD}. Its value can be experimentally evaluated at low temperature by using a thin crystal with very low Yb concentration, which fully prevents fluorescence reabsorption and Yb–Yb energy diffusion losses. Thus we have used a 0.08 at% (1 × 10^{19} at Yb cm^{-3}) Yb:CNGG crystal, obtaining τ_{RAD} = 816 μs, see the ESI† Fig. S14. This value is slightly larger than (and consistent with) fluorescence lifetimes previously reported for crystals with larger Yb concentration, 791 μs[42] for 5.77 at% Yb (2.3 × 10^{20} cm^{-3}) and 780 μs[39] for 2.8 at% Yb (1.1 × 10^{20} cm^{-3}) doping. On the other hand τ_{RAD} may be calculated from the $\sigma_{EMI}(\lambda)$ by the Füchtbauer–Ladenburg method[45] as $\tau_{RAD}^{-1} = 8\pi n^2 c \times \int(\sigma_{EMI}/\lambda^4)d\lambda$, where n is the refractive index, $n(\lambda$ = 980 nm) = 1.96,[19] and c is the speed of light in the vacuum. The calculated τ_{RAD} values using the above emission cross sections are τ_{RAD} = 440 μs for Yb:CNGG, τ_{RAD} = 464 μs for 12.23 at% Na-modified 7.13 at% Yb:CNNGG, and τ_{RAD} = 419 μs for Li-modified Yb:CLNGG. Taking into account the large number of parameters involved in these methodologies and the multisite character of the crystals, we consider that that experimental and calculated τ_{RAD} values agree, giving confidence to the present spectroscopic results.

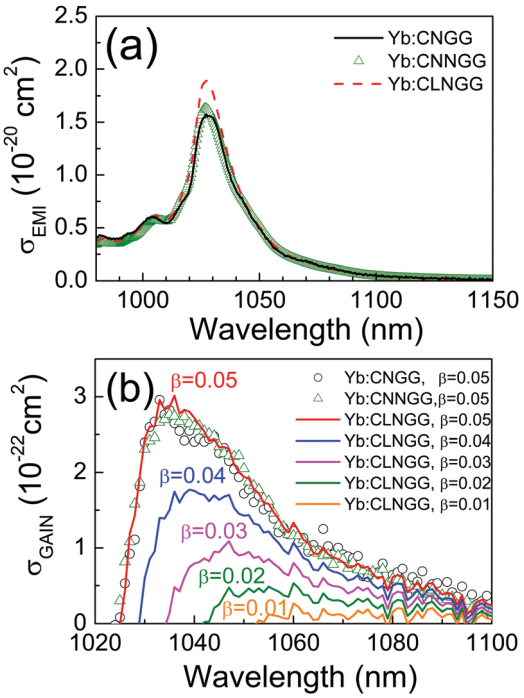

Fig. 5 (a) Emission cross section, σ_{EMI}, of Yb:CNGG-type crystals. (b) Gain cross sections of Yb:CNGG-type crystals. Circles are for Yb:CNGG, β = 0.05. Triangles are for Yb:CNNGG, β = 0.05. The lines correspond to Yb:CLNGG for different β values.

Since the ground $^2F_{7/2}$ laser level of Yb^{3+} is electronically populated at room temperature, the laser efficiency is determined by the competition between absorption and emission cross sections. The gain cross section, $\sigma_{GAIN} = \beta\sigma_{EMI} - (1-\beta)\sigma_{ABS}$ (β denotes the ratio of inverted ions to the total Yb density), describes this fact. Fig. 5b shows $\sigma_{GAIN}(\lambda)$ for Yb:CLNGG crystals. Very similar σ_{GAIN} distributions have been also found for Yb:CNGG and Yb:CNNGG, see Fig. 5b.

3d. Laser results

Along with laser experiments the sample pump absorption (either under laser operation or not) was evaluated from the beam passing through one of the cavity folding mirrors (a pumping mirror was used for this purpose). Systematic measurements were performed either under true continuous wave (cw) pumping or by 50%

 This journal is © The Royal Society of Chemistry 2021

Open Access Article. Published on 22 March 2021. Downloaded on 4/26/2024 4:27:57 AM.
This article is licensed under a Creative Commons Attribution-NonCommercial 3.0 Unported Licence.

modulation of the pump beam with a chopper, quasi continuous (qcw) pumping.

For low Yb concentration, pump absorption limits laser operation, but crystals with 1.74 at% Yb already showed laser action. While for high Yb concentration the radiative losses are the limit, consistently a 18.8 at% Yb:CNGG crystal grown using low purity precursors, *i.e.* 99.9% Yb_2O_3, 99.9% Nb_2O_5 and 99.5% $CaCO_3$ did not show laser action. In between these limits, laser operation was achieved independently of the growth conditions. Fig. 6a shows an example of the linear relation between the laser output power and the absorbed pump power obtained using different output coupler transmissions (T_{OC}). Laser performance is characterized by the slope of this relationship (η) and by the pump power laser threshold (P_{th}). Under these conditions laser output was unpolarized. For all tested crystals only minor differences were found between cw and qcw operation regimes, thus at the considered power levels, the sample heating was not a relevant factor. The laser slope efficiency increases with T_{OC} up to rather large values (η = 80% for the 7.28 at% Yb:CLNGG monitored crystal with T_{OC} = 10%) and the laser emission spectrum shifts to shorter wavelengths with T_{OC} increase, see Fig. 6b. This latter effect is consistent with the shift observed for σ_{GAIN} with increasing β, see Fig. 5b, and it is characteristic of three level lasers.

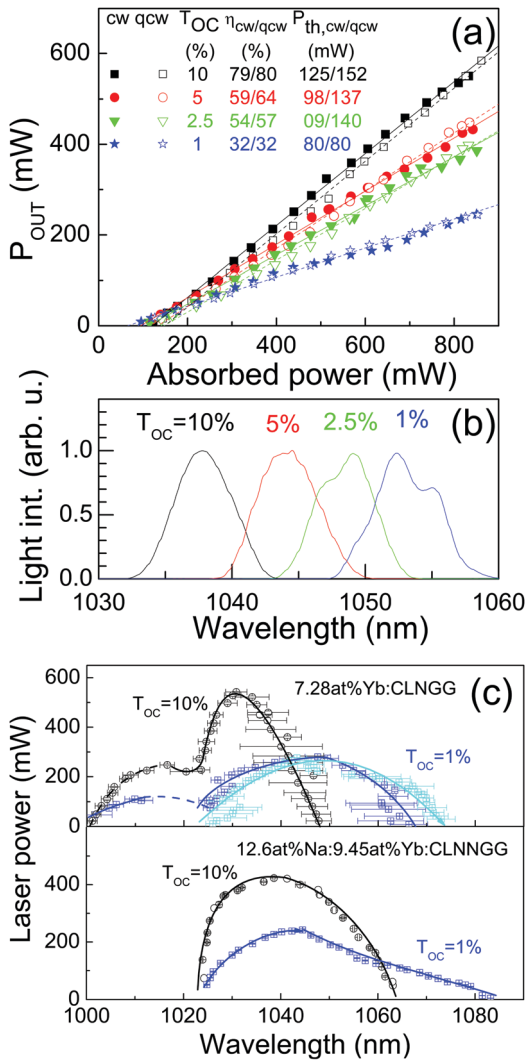

Fig. 6 Laser properties of Yb:CLNGG crystals for different output coupler transmissions, T_{OC}. (a) Input–output laser characteristics of the 7.28 at% Yb:CLNGG sample with thickness d = 2.05 mm. λ_{PUMP} = 972 nm. Open symbols, qcw, and full symbols, cw, laser operation. (b) Spontaneous laser emissions of the above crystal. (c) Laser tunability of 7.28 at% Yb:CLNGG crystals with thickness d = 0.824 (cyan, T_{OC} = 1%) and 2.05 mm (blue and black, T_{OC} = 1 and 10% respectively) and 12.56 at% Na: 9.45 at% Yb:CLNNGG crystal with thickness d = 1.37 mm. The lines are only a visual help.

A broad laser tuning range is a prerequisite for short laser pulses by mode-locking. Laser tuning of the crystals was studied by inserting at the Brewster angle a dispersive prism near to the rear mirror that forces a horizontally polarized laser output. In this case a high reflectance folding mirror was used opposite to the pumping mirror that recycled some of the transmitted pump, leading to slightly higher laser output powers. Fig. 6c shows the tuning range obtained for Yb-doped CLNGG and CLNNGG crystals using different output couplers.

It must be noted that at the peak of the tuning curves the emission is quite stable around a single wavelength (FWHM < 1.5 nm), but at the wings of the curves most typically several laser wavelengths with differences of up to $\Delta\lambda \approx 10$ nm coexist. This difference is represented in Fig. 6c by horizontal error bars. Consistently with the wavelength shift described above, tuning with T_{OC} = 1% extends more in the NIR (increasing λ) in comparison to the curves obtained with T_{OC} = 10%. With the 7.28 at% Yb:CLNGG crystal tuning ranges from λ = 1000 to 1075 nm thanks to the contribution of a secondary regime for λ < 1020 nm. It must be noted that lasing for λ < 1010 nm is limited by the coating design of the used optics with a cutoff at this wavelength. In the 12.56 at% Na: 9.45 at% Yb:CLNNGG crystal this secondary regime was not observed and laser emission started at λ = 1025 nm but by using T_{OC} = 1% it extends to λ > 1080 nm. These laser tuning spectral ranges widely exceed the 45 nm range (λ = 1030–1075 nm) previously reported with a Na-modified Yb:CNNGG crystal,[17] even though in this latter work a T_{OC} = 0.8% was used.

Since laser performance depends on many different material and instrumental parameters, in the following we study the relevance of some of them, such as crystal colouration, purity of used precursors, pump absorption and the effect of crystal modifications with Li or Na.

3d.i. Influence of $CaCO_3$ purity and crystal colouration on laser performance. The presence of point defects may affect the laser performance,[46,47] thus we have first compared the laser performance of Yb:CNGG-type crystals with different VIS and Red-NIR OAs. Fig. 7a and b show the laser slope efficiency and pump power laser threshold results, respectively, as a function of the Red-NIR OA (integral of the OA coefficient α from λ = 580 to 800 nm). Fig. 7c and d show similar results as a function of the VIS OA (α at λ = 400 nm). Although the scattering in the observed data could compromise conclusions, apparently the presence of the Red-NIR OA associated to the deep green colour seems to produce only a slight reduction of η and has no clear effect on P_{th}. On the other hand, the presence of some amount

Open Access Article. Published on 22 March 2021. Downloaded on 4/26/2024 4:27:57 AM.
This article is licensed under a Creative Commons Attribution-NonCommercial 3.0 Unported Licence.

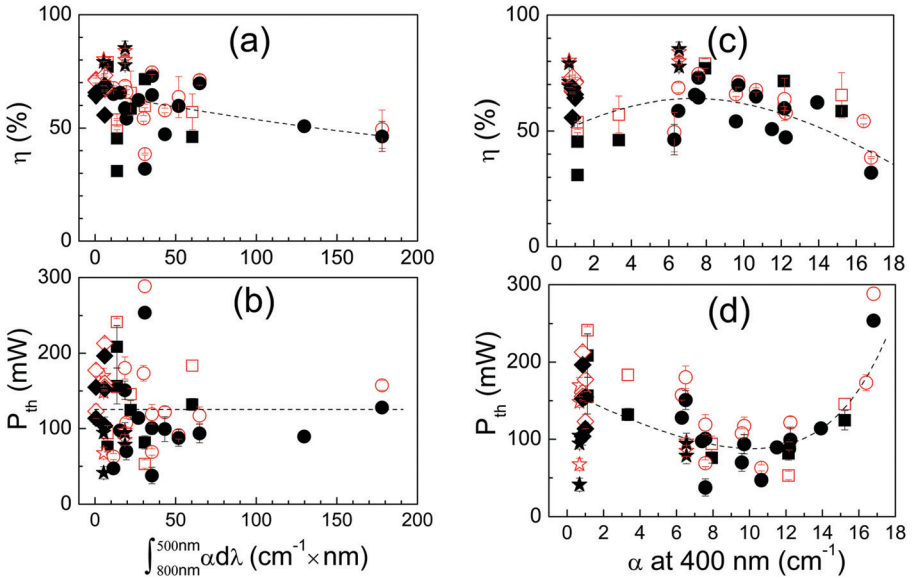

Fig. 7 Laser slope efficiency η (a and c) and pump power laser threshold P_{th} (b and d) of Yb:CNGG-type crystals *versus* Red-NIR (a and b) and VIS (c and d) crystal colouration. Squares, Yb:CNGG. Circles, Yb:CNNGG. Stars, Yb:CLNGG. Diamonds, Yb:CLNNGG. Open and full symbols correspond to qcw and cw results, respectively. T_{OC} = 10%.

of pre-edge OA in the visible region, associated to a yellow crystal colour, seems not to be harmful for laser performance and it seems to be even good in terms of maximizing η and minimizing P_{th}.

Since laser colouration is mostly related to the purity of the used $CaCO_3$, Fig. 8 shows a comparison of the laser performance for ≈9 at% Yb:CNGG crystals grown using 99.99% or 99.5% $CaCO_3$. No laser performance difference is found despite the fact that the integrated OA of the Red-NIR bands changes from 7.8 to 31 cm^{-1} × nm and that the pre-edge OA of both crystals was α(400 nm) = 7.9 and 12.1 cm^{-1}, respectively. A similar conclusion was also obtained for Na-modified ≈9 at% Yb:CNNGG, and for Li-modified ≈7.5 at% Yb:CLNGG, see the ESI,† Fig. S16. It can be concluded that, different to other laser crystal hosts, the defects responsible for the CNGG crystal colouration do not have much influence on the Yb^{3+} laser performance.

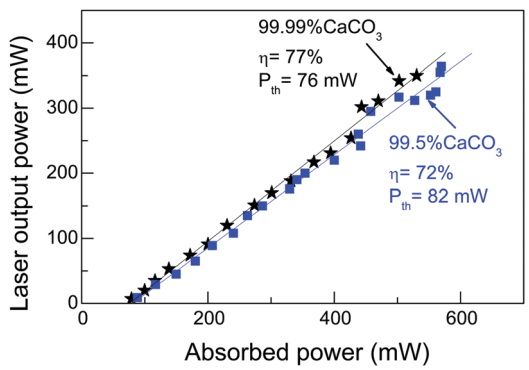

Fig. 8 Input–output cw laser characteristics of Yb:CNGG crystals grown by using $CaCO_3$ reagents with different purity: 9.01 at% Yb:CNGG grown with 99.99% $CaCO_3$ and 99.99% Nb_2O_5 (black stars), thickness d = 0.853 mm, λ_{PUMP} = 971.9 nm, *versus* 9.08 at% Yb:CNGG grown with 99.5% $CaCO_3$ and 99.95% Nb_2O_5 (blue squares), thickness d = 0.887 mm, λ_{PUMP} = 971.6 nm. 99.99% Yb_2O_3 purity was used in both cases. T_{OC} = 10%. The lines are linear fits of the experimental results.

3d.ii. Influence of Yb_2O_3 purity on laser performance. Although Yb^{3+} has no optical emission losses due to excited state absorption, trace amounts of Er and Tm (the two lanthanides with closest atomic numbers to Yb) are present even in the purest 99.998% Yb_2O_3 used. Because the excitation diffuses in the crystal by resonant energy transfer migration, these two impurities and other present point defects may reduce the Yb^{3+} radiative yield. This effect is expected to be more important as the Yb concentration increases.

In order to test the influence of Yb_2O_3 purity on the cw laser performance, two CNNG crystals with Yb concentration near 9.5 at% have been compared under as close as possible experimental conditions. The sample thickness was calculated to compensate the slight variation of the Yb concentration of the two samples in such a way that the pump absorption of the crystals under laser operation was close to each other and always in the 63–78% range. Fig. 9 shows the obtained results. For the crystal grown using 99.9% Yb_2O_3 reagent the slope efficiency was η_{CW} = 46% and η_{QCW} = 57% for the cw and qcw operation regimes, respectively. These magnitudes increase up to η_{CW} = 77% and η_{QCW} = 75% when 99.99% Yb_2O_3 reagent was used. In parallel, P_{th} decreases with increasing Yb_2O_3 purity, *i.e.* P_{th} = 167 mW and 75 mW for 99.9% and 99.99% Yb_2O_3 purity, respectively.

Another clue to understanding the influence of the Yb_2O_3 purity on laser operation is monitoring the Yb^{3+} lifetime. Generally, the high purity of Yb_2O_3 preserves the Yb^{3+} fluorescence yield,[48,49] which is beneficial for laser performance, however a decrease of the Yb^{3+} lifetime is expected with increasing Yb

 This journal is © The Royal Society of Chemistry 2021

Open Access Article. Published on 22 March 2021. Downloaded on 4/26/2024 4:27:57 AM.
This article is licensed under a Creative Commons Attribution-NonCommercial 3.0 Unported Licence.

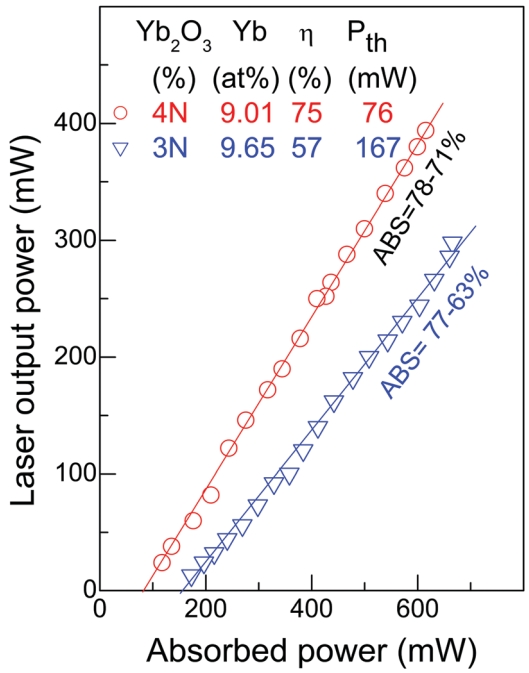

Fig. 9 Input–output characteristics of ≈9.5 at% Yb:CNGG-type crystals as a function of the Yb_2O_3 reagent purity under qcw pumping. Symbols are the experimental results and lines are their linear fits. Slope efficiencies, η, and power pump laser thresholds, P_{th}, are annotated in the figure inset. λ_{PUMP} = 971.8 nm. T_{OC} = 10%. Blue triangles, 99.9% (3N) Yb_2O_3, 9.65 at% Yb:CNGG, sample thickness d = 0.860 mm, pump absorption 77–63%. Red circles, 99.99% (4N) Yb_2O_3, 9.01 at% Yb:CNNGG, sample thickness d = 0.853 mm, pump absorption 78–71%.

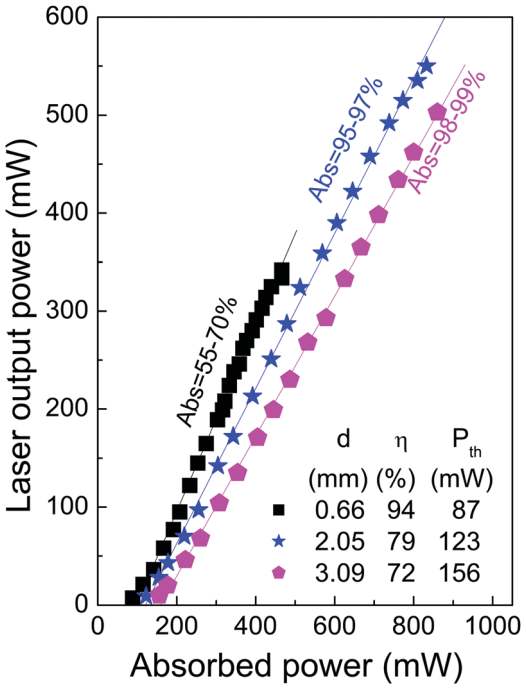

Fig. 10 Input–output cw laser characteristics of 7.3 at% Yb:CLNGG crystals with different sample thickness, d. λ_{PUMP} = 972.2 nm, T_{OC} = 10%. Abs = pump absorption under laser operation.

concentration due to Yb–Yb energy migration. This general trend is shown in the ESI,† Fig. S15. Thus it is important to compare only crystals with similar Yb concentration. The Yb^{3+} lifetime measured for a 9.65 at% Yb:CNGG crystal grown with 99.9% Yb_2O_3 was τ = 484 μs, but this value recovers to τ = 547 μs in 9.08 at% Yb:CNGG grown with 99.99% Yb_2O_3 purity. Similarly, the lifetime of a 12.07 at% Yb:CNGG crystal grown with 99.9% Yb_2O_3 was τ = 406 μs while that for a 12.6 at % Yb:CNNGG crystal grown with 99.99% Yb_2O_3 amounted to τ = 432 μs. Both, direct laser characterization and spectroscopic Yb^{3+} lifetimes indicate that as high as possible (at least 99.99%) Yb_2O_3 purity must be used to optimize laser operation of Yb:CNGG-type crystals.

3d.iii. Influence of pump absorption on laser performance. Efficient absorption of the pump beam is required for laser operation. This may be achieved by an appropriate combination of Yb concentration and sample thickness. Most Yb:CNGG lasers reported up to now used 5 at% Yb-doped crystals with 3 mm of thickness, see Table S1 (ESI†). However some laser designs, like the thin-disk lasers,[25,26] need thinner samples and therefore higher Yb concentrations. On the other hand, too thick samples would induce reabsorption of the laser emission and usually exceed the Rayleigh length of the focused pump beam, leading to poor coupling with the fundamental TEM00 cavity mode. Here we examine the combination of Yb concentration and sample thickness determining pump absorption.

Fig. 10 shows the input–output laser characteristics of a 7.3 at% Yb-doped CLNGG crystal with several sample thicknesses from d = 0.66 mm to 3.09 mm for T_{OC} = 10%. In all cases the emission was around λ = 1030 nm with a FWHM ≈ 2 nm. The largest slope efficiency (η ≈ 94%) was obtained for the thinnest used crystal, but the total output obtained in this case was limited to about 340 mW due to the low sample absorption (55–70% depending on pump power). For increasing crystal thickness the most evident trend is the increase of the pump power laser threshold. Maximum output power of 555 mW was achieved with a 2.05 mm crystal thickness with η = 79% and P_{th} = 123 mW for the λ = 972.2 nm pump beam, the absorption of this sample was 95–97%. A larger sample thickness tested, *i.e.* d = 3.09 mm, absorbs even more the laser pump power (98–99%) but the slope efficiency did not improve and the maximum output power was slightly lower, ≈500 mW. Therefore under the instrumental approach here used, pump absorption during laser operation in the 95–98% range seems optimal, which corresponds to 98% of absorption under low pump irradiation conditions.

An alternative way to increase laser pump absorption is by using larger Yb density in the crystal, and this is particularly desired if a small crystal thickness is required, however at some point the radiative yield of Yb^{3+} degrades with increasing Yb concentration, see Fig. S15 (ESI†). Fig. 11a and b show the effect of the Yb concentration on the laser slope efficiency and laser emission wavelength, respectively, for a near to constant pump absorption of 70–80% under laser operation, obtained by thickness selection. All crystals used for this comparison were grown

Open Access Article. Published on 22 March 2021. Downloaded on 4/26/2024 4:27:57 AM.
This article is licensed under a Creative Commons Attribution-NonCommercial 3.0 Unported Licence.

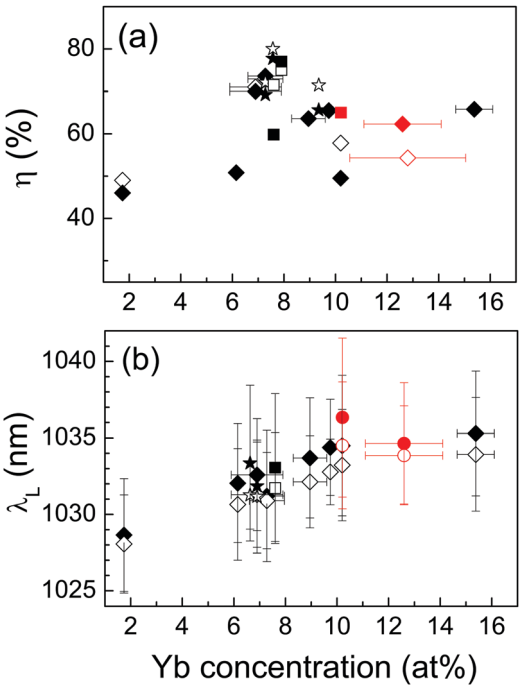

Fig. 11 Evolution of the laser performance of Yb:CNGG-type crystals with Yb concentration for a nearly constant pump absorption in the 70–80% range. Yb:CNGG (squares, λ_{PUMP} = 971.6 nm), Yb:CNNGG (diamonds, λ_{PUMP} = 971.9 nm) and Yb:CLNGG (stars, λ_{PUMP} = 972.2 nm). T_{OC} = 10%. Black and red symbols correspond to crystals grown with 99.99% and 99.995% Yb_2O_3 purity, respectively. (a) Laser slope efficiency, η. Open and full symbols correspond to qcw and cw operation, respectively. (b) Laser wavelength, λ_L. Open and full symbols correspond to near threshold and maximum pump absorption operation, respectively.

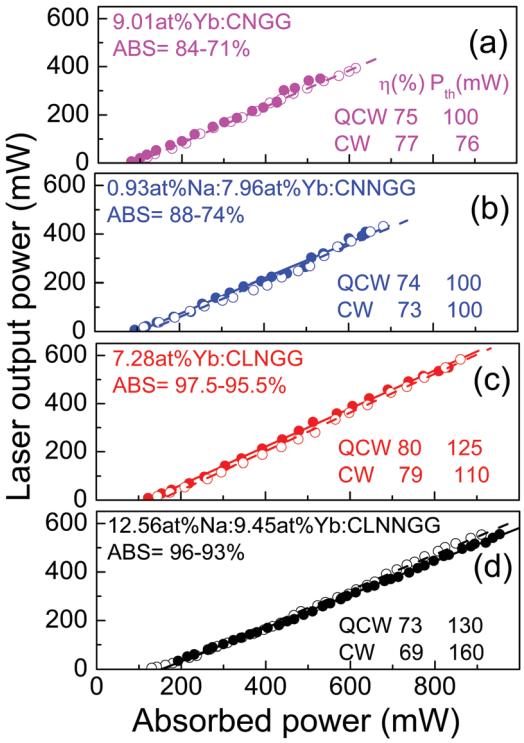

Fig. 12 Comparison of the laser performance of Yb:CNGG-type crystals with different modifiers under cw (full symbols and lines) and qcw (open symbols and dashed lines) operation regimes. T_{OC} = 10%. (a) Unmodified 9.01 at% Yb:CNGG, sample thickness d = 0.853 mm, λ_{PUMP} = 971.9 nm. (b) Na-modified 0.93 at% Na:7.96 at% Yb:CNNGG, sample thickness d = 1.371 mm, λ_{PUMP} = 971.6 nm. (c) Li-modified 7.28 at% Yb:CLNGG, sample thickness d = 2.05 mm, λ_{PUMP} = 972.2 nm. (d) Na and Li co-modified 12.56 at% Na: 9.45 at% Yb:CLNNGG, sample thickness d = 1.370 mm, λ_{PUMP} = 972.2 nm.

with ≥99.99% of Yb_2O_3 precursor purity. The laser slope efficiency increases from η = 47% in 1.74 at% Yb:CNNGG crystal to about η = 75% in crystals with 7–8 at% Yb. For larger Yb concentrations, up to about 15.4 at% of Yb doping, the laser slope efficiency decreases but still values around η = 60% were obtained. For all these crystals the laser threshold pump power remains in the P_{th} = 60–135 mW range, quite independent of the Yb concentration.

The increase of the Yb concentration also has a notable effect on the laser emission wavelength, see Fig. 11b. Although in fact the laser wavelength shifts for ≈1 nm to larger values as the pumping power increases from the threshold to the maximum pumping power available ≈1 W, the increase of the Yb concentration has a more notable effect shifting the spontaneous laser emission from λ_L = 1028 nm up to about λ_L = 1035 nm (for T_{OC} = 10%) as the Yb concentration changes from 1.7 at% to ≈15 at%.

3d.iv. Influence of Li or/and Na CNGG modifications on laser performance. Apart from the crystallographic and spectroscopic changes described in previous sections, here we aim to determine whether the different known modifications of the CNGG crystal, namely Li or Na modifications, have any impact on the laser performance of Yb:CNGG-type crystals. For this purpose we have compared four different Yb:CNGG-type crystals under as close as possible experimental conditions. These crystals are either unmodified Yb:CNGG, Na-modified Yb:CNNGG, Li-modified Yb:CLNGG, or Li and Na co-modified Yb:CLNNGG crystals. Although all these crystals were equally doped with 8 at% of Yb in the melt, the composition in the crystal varies according to that described previously ranging from minimum 7.28 at% Yb:CLNGG to maximum 9.45 at% Yb:CLNNGG (with 12.56 at% of Na). To achieve nearly constant pump absorption in the samples, different thicknesses were prepared for compensation of the different Yb densities. Despite this care, lower pump absorption was determined for the Yb:CNGG and Yb:CNNGG tested crystals which, accordingly to section 3d.iii, leads to the lower pump power laser thresholds and output powers.

Fig. 12 shows the laser performance of these four crystals. The slope efficiencies observed are in all cases in the η = 70–80% range, with very little difference between the qcw or cw operation regimens, i.e the effect of CNGG modifications on cw laser performance is weak, although still the largest slope efficiency is generally found for crystals modified with Li.

4. Discussion

CNGG-type single crystals are without doubt one of the crystalline laser media with largest emission bandwidths for lanthanides and in fact it is one of the few Yb-doped media that have produced sub

 This journal is © The Royal Society of Chemistry 2021

Open Access Article. Published on 22 March 2021. Downloaded on 4/26/2024 4:27:57 AM.
This article is licensed under a Creative Commons Attribution-NonCommercial 3.0 Unported Licence.

50 fs laser pulses, along with Yb:Ca(Y/Gd)AlO_4 (CALGO),[50–52] Yb:$Ca_4YO(BO_3)_3$ (YCOB),[53] Yb:$NaY(WO_4)_2$,[54] and Yb:CaF_2,[55] thus knowledge about the preparation and characterization of these garnets is relevant both from fundamental and technological view-points. Different to CALGO and YCOB, CNGG is optically isotropic, which is a significant advantage for crystal production and enables ceramic processing. In comparison to the present garnet, laser operation of Yb:$NaY(WO_4)_2$ is limited by lower thermal conductivity, $\kappa < 1.8$ W m^{-1} K^{-1}.[56] Although the laser capability of the CNGG crystal has been known for more than 30 years,[57] the information so far available on preparation, growth and characterization is still scarce due to the complexity of the crystal site filling and in particular, laser results obtained with different crystal compositions and experimental setups are difficult to compare, thus the real influence of the differences found in tested crystals on laser performance is not conclusive.

The incorporation of Li^+ is the classical crystal modifier.[22,23,58] The incorporation of Na^+ is a more recent and apparently successful proposal;[21] note that the shortest Yb laser pulses reported for these garnets were achieved with a Na-modified Yb:CNNGG crystal.[17] Both alkaline metals play an utterly different role in the crystalline structure and thus in the physical properties. Complementary MAS-NMR and neutron diffraction studies[19] showed that Li^+ incorporates exclusively in the tetrahedral site (not shared with the octahedral position as usually speculated without experimental evidence), while as determined by scXRD measurements Na^+ incorporates exclusively in dodecahedral sites, see Table 1 and ref. 21. Na^+ and Yb^{3+} codoping in equal amounts in substitution of two Ca^{2+} ions was thought to be a charge and elastic stress self-compensation method since the three ions sit on the same crystal site, but Fig. 1 shows that Na and Yb have quite different segregation coefficients, $S_{Na} \approx 0.39$ and $S_{Yb} > 1$, respectively. Therefore, the appropriate self-compensation cannot be obtained by using equal amounts of Na and Yb in the melt, as so far tried. Results shown in section 3a indicate that by using a ≈3Na:1Yb molar ratio in the melt, Na and Yb concentrations equalize in the crystal, leading to true self-compensation and this procedure indeed enhances the Yb incorporation to the crystal by slightly increasing the Yb segregation coefficient from $S_{Yb} = 1.12$ in Yb:CNGG crystals to $S_{Yb} = 1.34$ in Yb:CNNGG ones, in both cases larger than the Yb segregation coefficient in YAG, $S_{Yb}(YAG) = 1.08$.[59] On the contrary the segregation of Yb in Li-modified CLNGG reduces to $S_{Yb} = 0.88$, which is not so surprising because both Yb^{3+} and Li^+ incorporations suppose extra electric charge with regards to the substituted ions, Ca^{2+} and neutral tetrahedral vacancies, respectively.

One important consideration in the development of laser crystals is the cost of growth production and manufacturing. In this respect the purity of the required chemicals plays a key role. In Section 3b it was shown that the use of 99.5% $CaCO_3$ purity induces crystal colouration thus the more expensive 99.99% purity is required to minimize it. Other crystal growth procedures, particularly the growth in non-oxidative atmosphere required by the use of iridium crucibles, may also contribute with additional crystal colouration.[35] In our experience the colouration described here in Section 3b, Fig. 3, is permanent as it was not removed by after growth crystal annealing in air upon cooling, or by subsequent 1340 °C annealing in air (see the ESI,† Fig. S7). We have even observed that 1150 °C air annealing of Yb:CNGG-type ground crystals leads systematically to a decrease of the Yb^{3+} fluorescence lifetime, see the ESI† Fig. S17. However, in light of the results presented in Fig. 7 and 8 for the Yb:CNGG-type crystals the impact of this colouration in the Yb laser performance is minor. This can be attributed to several facts: Firstly, neither the pump ($\lambda_{PUMP} \approx 972$ nm) nor laser emission (λ_L = 1030–1080 nm) wavelengths characteristic of Yb^{3+} lasers overlap the defect-related VIS (λ = 300–500 nm) or Red-NIR (λ = 580–800 nm) OA bands responsible for the crystal colouration. This conclusion must be taken with care when considering other laser lanthanides, such as NIR Tm^{3+} and Nd^{3+} lasers (pumped at $\lambda \approx 800$ nm),[60,61] or VIS lasers based in Pr^{3+} (λ_{EXC} = 485 nm and λ_{EMI} = 595 and 640 nm), Tb^{3+} (λ_{EXC} = 488 nm and λ_{EMI} = 542 and 587 nm) or Dy^{3+} (λ_{EXC} = 425–475 nm and $\lambda_{EMI} \approx$ 580nm).[62] Secondly, the Yb^{3+} lifetime reduction observed with increasing crystal colouration is smaller than 10%,[19] thus it likely has a minor effect on the Yb^{3+} fluorescence yield and on laser performance. Thirdly, the cubic centrosymmetric garnet structure lacks the electro-optic Pockels effect thus any microscopic electric field caused by electron photo-excitation and diffusion has virtually no effect on the beam propagation controlled by a single refractive index value, only the very weak Kerr effect would contribute to refractive index changes. Fourthly, any thermal gradient induced by light absorption in these colour centres is symmetric, thus it must be easier to handle than for highly anisotropic crystals, *e.g.* monoclinic Yb:$KLn(WO_4)_2$ lasers.[63]

Undoped CNGG-type crystals can be grown with a microscopic crystallographic quality as good as that of commercial YAG crystals, see Fig. 2b. However, while full Yb solubility is found in the YAG case, *i.e.* Y can be completely substituted by Yb leading to YbAG crystals, in the CNGG case DSC and XRD results presented in section 3a have shown that the maximum substitution of Ca is about 20% of the atomic content of the dodecahedral position. This limit could be maybe enhanced by incorporation in the dodecahedral site of other divalent cations with ionic radius smaller than Ca^{2+}, but at present 15 at% Yb incorporation is a real limit for Yb:CNGG-type crystals with laser quality. Furthermore, Yb incorporation generally increases crystal mosaicity (see Fig. 3b), enhances fluorescence reabsorption and reduces the Yb^{3+} fluorescence quantum efficiency (fluorescence lifetime reduction with increasing Yb concentration, see Fig. S15, ESI†). Thus specific care must be paid to Yb incorporation in CNGG grown for laser purposes.

What makes a significant difference in laser performance is the Yb_2O_3 purity used for crystal growth. Fig. 9 shows the reduced laser slope efficiency found for 9.65 at% Yb:CNGG crystals grown with 99.5% Yb_2O_3 purity and, as mentioned previously, the only crystal which did not operate as a laser was a 18.8 at% Yb:CNGG crystal grown with 99.5% Yb_2O_3 purity. For such high Yb concentrations the fluorescence lifetime reduces to less than half of the radiative value, see Fig. S14 and S15 (ESI†). Care must be taken with some lifetime values reported in the Yb:CNGG literature[32] because despite the large Yb concentration

Open Access Article. Published on 22 March 2021. Downloaded on 4/26/2024 4:27:57 AM.
This article is licensed under a Creative Commons Attribution-NonCommercial 3.0 Unported Licence.

of the used crystals and the use of pin hole methods they exceed the radiative value most likely due to fluorescence reabsorption.

The impact of the crystal modifications on qcw/cw laser performance of 7.28–9.45 at% Yb:CNGG-type crystals here examined is rather small. The observed differences could be attributed to difficulty in controlling day-to-day fluctuations in the experimental conditions or in sample preparation, for instance perfection of the cavity alignment, fluctuations of the Ti-sa beam quality, accuracy of sample face flatness and parallelism or quality of the sample face polishing. Nevertheless, the comprehensive analysis of all the results here presented suggests that under similar conditions Li-modified Yb:CLNGG crystals have slightly better laser performances than the others, see Fig. 11a and Fig. 12, which agrees with the conclusion of ref. 24. This prevalence has not an optical spectroscopic support since emission and gain cross sections have been found independent of the Yb:CNGG Li or Na modifiers, see Fig. 5a and b, which points to the fact that the 300 K Yb^{3+} fluorescence is controlled by the main Yb^{3+} centre, in all cases a dodecahedral Yb^{3+} surrounded by six GaO_4 tetrahedra. A better crystalline quality could be the likely reason for the slightly improved Yb:CLNGG laser performance. It must be noted that despite its spontaneous nucleation on Pt wires, Li-modified Yb:CLNGG crystals exhibit a mosaicity lower than that observed in other Yb:CNGG-type compositions with similar Yb concentration, see Fig. 2b.

Mode-locking laser experiments using semiconductor saturable absorption mirrors (SESAM) as rear high reflectors benefit from low transmission output couplers ($T_{OC} \leq 1\%$) to increase the optical fluence onto the SESAM. Fig. 6b shows that this shifts the spontaneous emission laser wavelength towards larger values. Accordingly, previous Yb:CNGG-type crystals have shown mode-locking pulses in the λ = 1047.5–1061 nm region, see Table S1 (ESI†). Fig. 6c shows an unprecedented large cw laser tuning range for 12.56 at% Na:9.45 at% Yb:CLNNGG crystals, extending beyond $\lambda > 1080$ nm with a smooth variation of the output power in the long wavelength wing. The shortest pulses (τ = 45 fs) so far reported for Yb:CNGG-type crystals[17] were achieved with a T_{OC} = 0.8% and a Yb:CNNGG crystal doped in the melt with 10 at% Na ($\approx$4 at% Na in the crystal in light of our results) and 10 at% Yb, they were centred at 1061 nm with a FWHM of 26.8 nm, *i.e.* near to the long wavelength limit of the tuning curves shown in Fig. 6c for T_{OC} = 1%, however the average laser output was only 30 mW. While $\sigma_{GAIN} > 0$ is still found for λ = 1100 nm, see Fig. 5b, for $\lambda \geq 1040$ nm its spectral distribution is not modified by Li or Na incorporations, thus further improvements (shorter pulses and larger average output power) should be still expected by optimizing the crystal laser properties along the lines here described, *i.e.* maximizing laser performance by selecting Yb concentration in the 7–8 at% range, pump absorption to $\approx$95%, and reducing crystal mosaicity by the use of high crystalline quality seeds for growth and Li incorporation. Also, common Ti-sa laboratory lasers are limited to <2 W for λ = 972 nm, thus the use of Distributed Bragg Reflector DL (DBR-DL) with stabilized emission near the 972 nm would benefit the slightly larger peak σ_{ABS} shown in Fig. 5a while providing the high fluence needed by the used SESAM.

Thin-disk lasers[25,26] use crystal wafer thickness in the order of d = 100 μm for efficient cooling. One important aspect in this respect is the efficient absorption of the pumping without the need to increase the sample thickness. According to the results shown in Fig. 11a this seems possible in CNGG by using Yb doping levels between 10 and 15 at%, but direct Yb incorporation increases crystal mosaicity, Fig. 2b. This mosaicity can be reduced by Li modification, but this in turn reduces Yb incorporation. Although Na incorporation also increases the crystal mosaicity it is still a useful strategy to promote Yb incorporation to high levels, $\approx$15 at%, thus Li and Na co-modified Yb:CLNNGG crystals seem a promising direction for future improvements of the efficiency of these lasers.

Transparent ceramic processing of CNGG garnets remains challenging,[18] but in light of the results presented in Fig. S9 (ESI†), vacuum annealing at high temperature should be avoided in order to minimize Ga loss that presumably gives rise to foreign crystallographic phases at the grain boundaries.

5. Conclusions

CNGG single crystals can be grown by the Czochralski method up to $\approx$20 at% of Ca substitution by Yb and Na. The segregation coefficients for Yb and Na are rather different, namely S_{Yb} = 1.12 ± 0.11 for Yb (S_{Yb} = 1.34 ± 0.09 in Yb and Na codoped crystals) and S_{Na} = 0.39 ± 0.05 for Na. Li reduces the Yb segregation coefficient below one, S_{Yb} = 0.88 ± 0.07. Similar Na and Yb densities in the crystal require a 3Na : 1Yb atomic ratio in the melt. The incorporation of Yb and Na into the garnet structure of CNGG crystals leads to a slight increase of the crystalline mosaicity, which can be compensated by Li incorporation as well as by the use of seeds with high crystalline quality, for instance YAG. Li and Na are complementary modifications of the garnet CNGG structure that help to simultaneously control the Yb incorporation and crystalline quality. Slightly better cw laser performance has been found in Li-modified Yb:CLNGG crystals while NIR extended laser tuning was observed in Li and Na co-modified Yb:CLNNGG crystals.

The purity of chemical precursors, in particular $CaCO_3$, is crucial to reduce the sample colouration associated with broad optical absorption bands appearing in the λ = 580–800 nm spectral range and with a band in the pre-edge (λ = 300–500 nm, peaking at λ = 350 nm) of the band gap transition. These two optical absorptions correspond to different optical centres apparently not related to oxygen deficiency, but their presence does not have a great influence on the cw laser performance of Yb^{3+} in the studied garnet host. However, the use of high purity Yb_2O_3 chemical is critical to preserve the radiative properties of Yb^{3+} thus to maximize the cw laser slope efficiency and to reduce the pump power laser threshold.

A statistical assessment of the Yb^{3+} absorption cross section provides peak values of $\sigma_{ABS}(\lambda = 971.7\ nm) = 1.97 \pm 0.32 \times 10^{-20}\ cm^2$ for Yb:CNGG, $\sigma_{ABS}(\lambda = 971.8\ nm) = 1.65 \times 10^{-20}\ cm^2$ for 12.23 at% Na-modified Yb:CNNGG and $\sigma_{ABS}(\lambda = 972.1\ nm) = 2.12 \pm 0.34 \times 10^{-20}\ cm^2$ for Li-modified Yb:CLNGG. No evidence of significant

 This journal is © The Royal Society of Chemistry 2021

Open Access Article. Published on 22 March 2021. Downloaded on 4/26/2024 4:27:57 AM.
This article is licensed under a Creative Commons Attribution-NonCommercial 3.0 Unported Licence.

emission or gain cross section changes with the incorporation of Li or Na modifiers is found. $\sigma_{GAIN} > 0$ is found even for $\lambda \geq$ 1100 nm. By using different output coupler transmissions and crystal compositions, laser tuning was possible in a very broad spectral range, from λ = 1000 nm to beyond λ = 1080 nm, suggesting that the full capability of these crystals for the production of ultrashort laser pulses has not yet been completely exploited.

Author contributions

All authors contributed to Conceptualization, Investigation, Data analysis and Funding acquisition. The manuscript was written through contributions of all authors.

Conflicts of interest

There are no conflicts to declare.

Acknowledgements

Work supported by MICINN under project number RTI2018-094859-B-I00. EPMA analyses have been performed by A. Fernández Larios at Centro Nacional de Microscopía Electrónica of Universidad Complutense de Madrid. CSIC support for Open Access publication as well as that of P. Ortega and M. J. Velasco (ICV-CSIC) in WDXRF and J. Perles and M. Ramírez (SIdI-UAM) in scXRD measurements are acknowledged.

References

1 U. Keller, *Appl. Phys. B: Lasers Opt.*, 2010, **100**, 15.
2 V. C. Coffey, *Opt. Photonics News*, 2014, 30.
3 M. Arrigoni, S. Butcher and J. Henrich, *Laser Focus Word*, 2020, 56.
4 M. Smrž, O. Novák, J. Mužík, H. Turčičová, M. Chyla, S. S. Nagisetty, M. Vyvlečka, L. Roškot, T. Miura, J. Černohorská, P. Sikocinski, L. Chen, J. Huynh, P. Severová, A. Pranovich, A. Endo and T. Mocek, *Appl. Sci.*, 2017, **7**, 1016.
5 W. Sibbett, A. A. Lagatsky and C. T. A. Brown, *Opt. Express*, 2012, **20**, 6989.
6 T. Südmeyer, C. Kränkel, C. R. E. Baer, O. H. Heckl, C. J. Saraceno, M. Golling, R. Peters, K. Petermann, G. Huber and U. Keller, *Appl. Phys. B: Lasers Opt.*, 2009, **97**, 281.
7 S. Uemura and K. Torizuka, *Jpn. J. Appl. Phys.*, 2011, **50**, 010201.
8 A. Ikesue and Y. L. Aung, *J. Am. Cer. Soc.*, 2006, **89**, 1936.
9 J. Sanghera, W. Kim, G. Villalobos, B. Shaw, C. Baker, J. Frantz, B. Sadowski and I. Aggarwal, *Materials*, 2012, **5**, 258.
10 S. Chen and Y. Wu, *Am. Ceram Soc. Bull.*, 2013, **92**, 32.
11 O. Puncken, H. Tünnermann, J. J. Morehead, P. Weßels, M. Frede, J. Neumann and D. Kracht, *Opt. Express*, 2010, **18**, 20461.
12 D. Albach and J. Chanteloup, *Opt. Express*, 2015, **23**, 570.
13 L. Zhang, J. Wu, P. Stepanov, M. Haseman, T. Zhou, D. Winarski, P. Saadatkia, S. Agarwal, F. A. Selim, H. Yang, Q. Zhang, Y. Wang, C. Wong and H. Chen, *Photonics Res.*, 2019, **7**, 549.
14 J. Akiyama, Y. Sato and T. Taira, *Opt. Lett.*, 2010, **23**, 3598.
15 H. Furuse, N. Horiuchi and B. Kim, *Sci. Rep.*, 2019, **9**, 10300.
16 M. Tokurakawa, A. Shirakawa, K. Ueda, H. Yagi, T. Yanagitani and A. A. Kaminskii, *CLEO/IQEC*, 2009, CFO3.
17 J. Ma, Z. Pan, J. Wang, H. Yuan, H. Cai, G. Xie, L. Qian, D. Shen and D. Tang, *Opt. Express*, 2017, **25**, 14968.
18 V. Lupei, A. Lupei, C. Gheorghe, L. Gheorghe, A. Achim and A. Ikesue, *J. Appl. Phys.*, 2012, **112**, 063110.
19 M. D. Serrano, J. O. Álvarez-Pérez, C. Zaldo, J. Sanz, I. Sobrados, J. A. Alonso, C. Cascales, M. T. Fernández-Díaz and A. Jezowski, *J. Mater. Chem. C*, 2017, **5**, 11481.
20 J. O. Álvarez-Pérez, J. M. Cano-Torres, M. D. Serrano, C. Cascales and C. Zaldo, *J. Mater. Chem. C*, 2020, **8**, 7882.
21 E. Castellano-Hernández, M. D. Serrano, R. J. Jiménez-Riobóo, C. Cascales and C. Zaldo, *Cryst. Growth Des.*, 2016, **16**, 1480.
22 A. A. Sobol, *Proc. Indian Natl. Sci. Acad.*, 1991, **57**, 125.
23 Y. K. Voronko, A. A. Sobol, A. Y. Karasik, N. A. Eskov, P. A. Rabochkina and S. N. Ushakov, *Opt. Mater.*, 2002, **20**, 197.
24 J. Liu, Y. Wan, Z. Zhou, X. Tian, W. Han and H. Zhang, *Appl. Phys. B: Lasers Opt.*, 2012, **109**, 183.
25 A. Giesen, H. Hugel, A. Voss, K. Wittig, U. Brauch and H. Opower, *Appl. Phys. B: Lasers Opt.*, 1994, **58**, 365.
26 A. Giesen and J. Speiser, *IEEE J. Sel. Top. Quantum Electron.*, 2007, **13**, 598.
27 J. I. Goldstein, D. E. Newbury, P. Echlin, D. C. Joy, A. Roming, C. Lyman, C. Fiori and E. Lifshin, *Scanning Electron Microscopy and X-ray Microanalysis*, Plenum. New York, 1992.
28 F. J. Valle, P. Ortega, A. de Pablos, C. Zaldo, F. Esteban-Betegón and M. D. Serrano, *X-Ray Spectrom.*, 2009, **38**, 287.
29 G. M. Kuz'micheva, I. A. Kaurova, A. A. Brykovskiy, V. B. Rybakov, Y. N. Gorobets, A. N. Shekhovtsov and A. Cousson, *Mater. Res. Bull.*, 2016, **78**, 134.
30 I. A. Kaurova, G. M. Kuz'micheva, V. B. Rybakov, A. B. Dubovskii and A. Cousson, *Inorg. Mater.*, 2010, **46**, 988.
31 G. M. Kuz'micheva, I. A. Kaurova, V. B. Rybakov, P. A. Eistrikh-Geller, E. V. Zharikov, D. A. Lis and K. A. Subbotin, *CrystEngComm*, 2016, **18**, 2921.
32 Z. Pan, P. Loiko, J. M. Serres, H. Yuan, X. Dai, H. Cai, M. Aguiló, F. Díaz, P. Camy, Y. Wang, U. Griebner, V. Petrov and X. Mateos, *Proc. SPIE*, 2020, **11259**, 1125911.
33 Z. Pan, P. Loiko, Y. Wang, Y. Zhao, H. Yuan, K. Tang, X. Dai, H. Cai, J. M. Serres, S. Slimi, E. B. Salem, E. Dunina, A. Kornienko, L. Fomicheva, J. Doualan, P. Camy, W. Chen, U. Griebner, V. Petrov, M. Aguiló, F. Díaz, R. M. Solé and X. Mateos, *J. Alloys Compd.*, 2021, **853**, 157100.
34 L. Gheorghe, M. Greculeasa, F. Voicu, C. Gheorghe, S. Hau, A. M. Vlaicu, K. N. Belikov, E. Yu Bryleva and O. V. Gaiduk, *Opt. Mater.*, 2018, **84**, 335.
35 Q. Fu, X. Liu, Y. Chen, C. Hong, X. Hu, N. Zhuang and J. Chen, *J. Alloys Compd.*, 2016, **660**, 471.
36 D. L. Wood and J. P. Remeika, *J. Appl. Phys.*, 1967, **38**, 1038.
37 C. R. Varney and F. A. Selim, *AIMS Mater Sci.*, 2015, **2**, 560.
38 O. F. Schirmer, *J. Phys.*, 1980, **41**, C6.479.
39 J. M. Serres, V. Jambunathan, P. Loiko, X. Mateos, H. Yu, H. Zhang, J. Liu, A. Lucianetti, T. Mocek, K. Yumashev,

Open Access Article. Published on 22 March 2021. Downloaded on 4/26/2024 4:27:57 AM.
This article is licensed under a Creative Commons Attribution-NonCommercial 3.0 Unported Licence.

U. Griebner, V. Petrov, M. Aguiló and F. Díaz, *Opt. Mater. Express*, 2015, **6**, 46.
40 V. E. Shukshin, *Phys. Wave Phenom.*, 2009, **17**, 165.
41 J. Liu, H. Yang, H. Zhang, X. Mateos, V. Petrov and J. Wang, *Laser Phys. Lett.*, 2008, **5**, 874.
42 H. Zhang, J. Liu, J. Wang, J. Fan, X. Tao, X. Mateos, V. Petrov and M. Jiang, *Opt. Express*, 2007, **15**, 9464.
43 J. Koerner, C. Vorholt, H. Liebetrau, M. Kahle, D. Kloepfel, R. Seifert, J. Hein and M. C. Kaluza, *J. Opt. Soc. Am. B*, 2012, **29**, 2493.
44 D. E. McCumber, *Phys. Rev. A: At., Mol., Opt. Phys.*, 1964, **136**, A954.
45 B. F. Aull and H. P. Jenssen, *IEEE J. Quantum Electron.*, 1982, **18**, 925.
46 D. Sugak, A. Matkovskii, A. Durygin, A. Suchocki, I. Solskii, S. Ubizskii, K. Kopczynski, Z. Mierczyk and P. Potera, *J. Lumin.*, 1999, **82**, 9.
47 X. Han, M. Rico, M. D. Serrano, C. Cascales and C. Zaldo, *Laser Phys. Lett.*, 2013, **10**, 045808.
48 V. Müller, V. Peters, E. Heumann, M. Henke, K. Petermann and G. Huber, *Adv. Sol. St. Lasers Tech. Dig.*, 2002, 153.
49 F. Esteban-Betegón, C. Zaldo and C. Cascales, *Chem. Mater.*, 2010, **22**, 2315.
50 F. Pirzio, S. D. di Dio Cafiso, M. Kemnitzer, A. Guandalini, F. Kienle, S. Veronesi, M. Tonelli, J. A. der Au and A. Agnesi, *Opt. Express*, 2015, **23**, 9790.
51 Z. Gao, J. Zhu, J. Wang, Z. Wei, X. Xu, L. Zheng, L. Su and J. Xu, *Photonics Res.*, 2015, **3**, 335.
52 S. Manjooran and A. Major, *Opt. Lett.*, 2018, **43**, 2324.
53 A. Yoshida, A. Schmidt, V. Petrov, C. Fiebig, G. Erbert, J. Liu, H. Zhang, J. Wang and U. Griebner, *Opt. Lett.*, 2011, **36**, 4425.
54 J. Ma, H. Huang, H. Yu, H. Zhang and D. Tang, *IEEE Photon Tech. Lett.*, 2016, **28**, 1298.
55 W. P. Sévillano, G. Machinet, R. Dubrasquet, P. Camy, J. L. Doualan, R. Moncorgé, P. Georges, F. Druon, D. Descamps and E. Cormier, *Adv. Sol. St. Lasers Tech. Dig.*, 2013, AF3A.6.
56 M. D. Serrano, C. Cascales, X. Han, C. Zaldo, A. Jezowski, P. Stachowiak, N. Ter-Gabrielyan, V. Fromzel and M. Dubinskii, *PLoS One*, 2013, **8**, e59381.
57 A. A. Kaminski, E. L. Belokoneva, A. V. Butashin, K. Kurbanov, A. A. Markosyan, B. V. Mill, O. K. Nikol'sakaya and S. E. Sarkisov, *Inorg. Mater.*, 1986, **22**, 1061.
58 Y. M. Yu, V. I. Chani, K. Shimamura and T. Fukuda, *J. Cryst. Growth*, 1997, **171**, 463.
59 X. Xu, Z. Zhao, J. Xu and P. Deng, *J. Cryst. Growth*, 2003, **255**, 338.
60 J. M. Cano-Torres, M. Rico, X. Han, M. D. Serrano, C. Cascales, C. Zaldo, V. Petrov, U. Griebner, X. Mateos, P. Koopmann and C. Kränkel, *Phys. Rev. B: Condens. Matter Mater. Phys.*, 2011, **84**, 174207.
61 A. García-Cortés, C. Cascales, A. de Andrés, C. Zaldo, E. V. Zharikov, K. A. Subbotin, S. Bjurshagen, V. Pasiskevicius and M. Rico, *IEEE J. Quantum Electron.*, 2007, **43**, 157.
62 C. Kränkel, D. Marzahl, F. Moglia, G. Huber and P. W. Metz, *Laser Photonics Rev.*, 2016, **10**, 548.
63 E. Castellano-Hernández, X. Han, M. Rico, L. Roso, C. Cascales and C. Zaldo, *Opt. Express*, 2015, **23**, 11135.

 This journal is © The Royal Society of Chemistry 2021